MEMS-based thin-film solid-oxide fuel cells

Jihwan An, Joon Hyung Shim, Young-Beom Kim, Joong Sun Park, Wonyoung Lee, Turgut M. Gür, and Fritz B. Prinz

Thin-film solid-oxide fuel cells (TF-SOFCs) fabricated using microelectromechanical systems (MEMS) processing techniques not only help lower the cell operating temperature but also provide a convenient platform for studying cathodic losses. Utilizing these platforms, cathode kinetics can be enhanced dramatically by engineering the microstructure of the cathode/electrolyte interface by increasing the surface grain-boundary density. Nanoscale secondary ion mass spectrometry and high-resolution transmission electron microscopy studies have shown that oxygen exchange at electrolyte surface grain boundaries is facilitated by a high population of oxide-ion vacancies segregating preferentially to the grain boundaries. Furthermore, three-dimensional structuring of TF-SOFCs enabled by various lithography methods also helps increase the active surface area and enhance the surface exchange reaction. Although their practical prospects are yet to be verified, MEMS-based TF-SOFC platforms hold the potential to provide high-performance for low-temperature SOFC applications.

Introduction

Solid-oxide fuel cells (SOFCs) are efficient electrochemical devices that convert the chemical energy of a fuel into electrical energy and typically employ an extrinsically doped ceramic oxide electrolyte membrane to transport ions through its crystal lattice, while the electrons traverse the external circuit providing useful electrical work. Thin-film SOFCs based on processing techniques used for microelectromechanical systems (MEMS) offer an attractive platform to study contributions from rate-controlling processes (i.e., the slowest step in the rate processes that governs the overall fuel cell performance). Naturally, as one slow step is enhanced, the next slow step becomes the dominant factor in determining the overall cell performance. In particular, thin-film electrolyte membranes can help reduce ohmic losses to such an extent that cathode activation losses become dominant. As the rate of the hydrogen oxidation reaction at the anode is considerably faster than the cathodic reaction, this article focuses on expanding the understanding of the oxygen reduction reaction (ORR) at the cathode followed by oxide ion incorporation into the electrolyte (see the Introductory article in this issue). In principle, ORR involves the reduction of molecular oxygen to oxide ions, which are then incorporated into vacant sites (i.e., oxide ion vacancies) in the oxygen sublattice of the ceramic electrolyte membrane. Using advanced analytical methods with high spatial and energy resolution that allowed us to trace the path of oxygen during ORR, we were able to elucidate the role of surface grain boundaries in this important reaction.

This article draws heavily from major results and findings reported in recent articles by us. First, we briefly review MEMS-based SOFC fabrication techniques followed by fabrication of thin-film electrolyte membranes. As these cells typically operate at temperatures lower than 500°C, they feature an ionically conducting ceramic electrolyte membrane with porous platinum electrodes at the anode and the cathode. Next, we present two engineering strategies to enhance the cathode reaction, which is the rate-determining step in MEMS-based SOFC: engineering of

Jihwan An, Department of Mechanical Engineering, Stanford University, USA, and Seoul National University of Science and Technology, Korea; jihwanan@stanford.edu
Joon Hyung Shim, Department of Mechanical Engineering, Korea University, South Korea; shimm@korea.ac.kr
Young-Beom Kim, Department of Mechanical Engineering, Hanyang University, South Korea; ybkim@hanyang.ac.kr
Joong Sun Park, Argonne National Laboratory, USA; parkj@anl.gov
Wonyoung Lee, School of Mechanical Engineering, Sungkyunkwan University, South Korea; leewy@skku.edu
Turgut M. Gür, Department of Materials Science and Engineering, Stanford University, USA; turgut.gur@stanford.edu
Fritz B. Prinz, Departments of Mechanical Engineering and Materials Science and Engineering, Stanford University, USA; fbp@cdr.stanford.edu
DOI: 10.1557/mrs.2014.171

surface grain-boundary density and surface topology by three-dimensional structuring.

Fuel cell fundamentals

Ignoring gas phase mass transport limitations and electrical resistance losses along the external circuit elements, the operating voltage (V) of a SOFC is defined as:

$$V = V_{oc} - \eta_{act,anode} - \eta_{act,cathode} - \eta_{ohmic}, \quad (1)$$

where V_{oc} represents the open-circuit voltage (OCV) determined by thermodynamics, $\eta_{act,anode}$ and $\eta_{act,cathode}$ represent the activation losses at the anode and the cathode, respectively, and η_{ohmic} represents the ohmic loss across the electrolyte.[1] In the case of H_2/air SOFCs, the anode kinetics for H_2 oxidation is significantly faster than the ORR kinetics at the cathode.[2] As a result, the activation loss at the cathode and the ohmic loss across the electrolyte are two major losses that dominate the performance of H_2/air SOFCs. As the ohmic loss is inversely proportional to the thickness of the electrolyte, use of thin-film electrolyte membranes greatly reduces ohmic losses.

Indeed, MEMS-based SOFCs employ thin electrolytes with thicknesses ranging from tens to hundreds of nanometers, which minimizes the ohmic loss, leaving the cathodic activation loss due to the sluggish rate of ORR to dominate the total cell losses. The cathodic activation loss ($\eta_{act,cathode}$) can be expressed as the following Tafel equation (when the activation loss is sufficiently large):

$$\eta_{act,cathode} = \left(RT/\alpha n F\right) \ln\left(j/j_0\right), \quad (2)$$

where R is the ideal gas constant, T is the temperature, n is the number of moles of electrons transferred, F is Faraday's constant, α is the charge-transfer coefficient, j is the current density, and j_0 is the exchange current density. To minimize the activation loss, therefore, we should have a high exchange current density. The exchange current density, j_0, can be further expressed as:

$$j_0 = j_0'\left(A/A'\right), \quad (3)$$

where j_0' is the intrinsic exchange current density on a perfectly smooth surface, and A/A' is the surface area enhancement (actual surface area/projected area). That is, in order to have a high exchange current density, one should enhance j_0' or increase A/A' (i.e., use a higher surface area structure).

The useful operating voltages of MEMS-based SOFCs are largely dictated by the cathodic activation loss, as the contributions from the anode and the electrolyte are significantly smaller. Consequently, enhancement of the cathodic kinetic rates significantly affects the performance of thin-film SOFCs. In this regard,

MEMS-based SOFCs with thin-film electrolyte membranes provide a convenient platform as a research testbed for exploring surface engineering methodologies and strategies at the cathode interface to improve ORR kinetics.

MEMS-based thin-film membrane electrode assemblies

Membrane electrode assemblies (MEAs) built on MEMS-processed single crystal Si wafers can provide an effective platform and a powerful tool to study and understand the role of the cathode/electrolyte interface microstructure at the nanoscale on cathodic rate processes that dominate cell performance in thin-film SOFCs, especially at low operating temperatures. Separation of cathodic processes from ohmic losses naturally accentuates the limitations of the ORR kinetics and makes it easier to investigate mechanistic pathways for oxygen incorporation at the cathode/electrolyte interface.

MEMS-based SOFC MEA

Most of the reported MEMS-based micro-SOFCs are fabricated on silicon wafers (**Figure 1**).[3–20] In this architecture, the silicon wafer functions as a mechanical support for the MEA whose thickness ranges from hundreds of nanometers to micrometers. Huang et al. described a fabrication process to build a freestanding MEA on a silicon wafer as follows:[3] (1) SiN is deposited on both sides of the double-polished silicon wafer, (2) a thin-film electrolyte is deposited on the top side, (3) the bottom SiN is patterned, (4) the silicon wafer is wet-etched by potassium hydroxide (KOH) to open up windows at the bottom surface, (5) SiN is dry-etched on the top side, and (6) Pt electrodes are deposited on both sides for the anode and the cathode. The size of the opening at the bottom in step 3 determines the resulting size of the freestanding membrane. The silicon wafer may be patterned before step 1 so that the resulting membranes have high surface areas.[4,5,8,9] This is discussed in more detail in the section on grain boundary engineering. As alternate supports for the MEA, glass-ceramic,[21] porous Ni,[22] anodized aluminum oxide substrates,[23–26] Ni foil,[27] and yttria-stabilized zirconia (YSZ) foil[15] have also been studied. A comprehensive review of micro-SOFCs with various
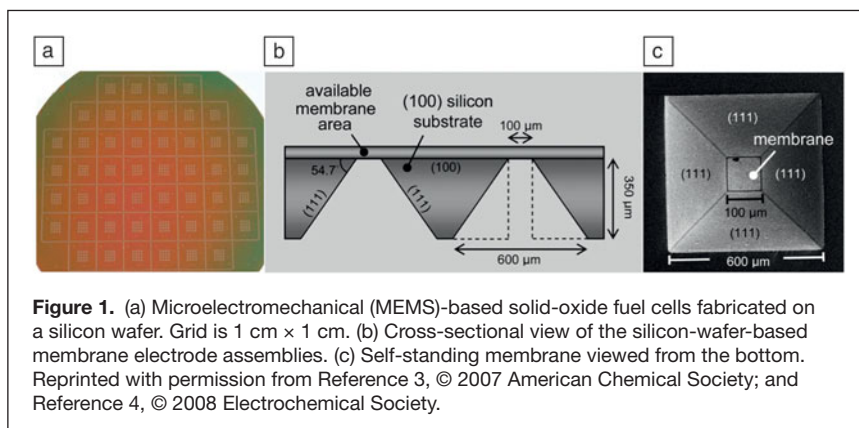

Figure 1. (a) Microelectromechanical (MEMS)-based solid-oxide fuel cells fabricated on a silicon wafer. Grid is 1 cm × 1 cm. (b) Cross-sectional view of the silicon-wafer-based membrane electrode assemblies. (c) Self-standing membrane viewed from the bottom. Reprinted with permission from Reference 3, © 2007 American Chemical Society; and Reference 4, © 2008 Electrochemical Society.

kinds of substrates, geometries, and cell performance results can be found in Reference 15.

Thin-film electrolyte membranes

One of the important characteristics of MEMS-based SOFCs is the employment of thin-film electrolytes. Two types of solid-oxide thin films have been widely used as electrolytes for MEMS-based SOFCs:[28,29] oxide-ion conducting oxides with a fluorite structure and proton-conducting oxides with a perovskite structure. Among oxide-ion conducting oxides, YSZ is the most popular electrolyte material for MEMS-based SOFCs as well as for larger-scale SOFCs. Even though the relatively low ionic conductivity of YSZ necessitates operation at high temperatures (800–1000°C), one can significantly lower the operating temperature down to less than 500°C by employing nanoscale thin-film YSZ membranes. Doped ceria, such as gadolinia-doped ceria (GDC) or yttria-doped ceria (YDC), are also frequently used as electrolytes.[3,11] Doped ceria electrolytes are known to be susceptible to the onset of electronic conductivity at elevated temperatures and low oxygen activities. On the cathode side, however, they have been used effectively as interlayers to facilitate oxygen reduction kinetics.

Perovskite-based proton-conducting oxides include yttria-doped barium zirconate (BZY) and yttria-doped barium cerate (BCY). They conduct protons through lattice oxygen vacancies via the Grotthuss mechanism (see the article by Fabbri et al. in this issue). Due to their low activation energy for proton transport and relatively high ionic conductivities compared to oxide-ion conducting ceramics with a fluorite structure, these doped perovskite-based proton conductors are interesting candidates for MEMS-based SOFC electrolytes.[7,30]

Thin-film electrolyte membranes for MEMS-based SOFCs have been deposited using various thin-film deposition tools, including sputtering, pulsed laser deposition (PLD), and atomic layer deposition (ALD).[29,31] RF sputtering was used to deposit thin-film membranes from oxide targets in an Ar-O$_2$ mixture environment.[3] Alternatively, DC sputtering can be used to deposit from metallic targets followed by annealing in O$_2$ or an air environment to form the oxide structures.[32] PLD is also a widely used tool to deposit thin-film electrolytes, in which the plume from a stoichiometric target that is ablated by an energetic laser pulse helps deposit the film on the heated substrate surface.[33–36] However, thin-film electrolytes fabricated by such methods as sputtering tend to have several issues when employed as electrolyte membranes for MEMS-based SOFCs. At film thicknesses of tens of nanometers, these membranes may show relatively high pinhole densities, resulting in electrical shorting between the top and the bottom electrodes, and/or chemical shorting between the fuel side (anode) and the oxygen side (cathode).

Conversely, pinhole-free uniform thin membranes can be fabricated by ALD, which is a surface-reaction-limited chemical vapor deposition process that enables surface conformal deposition of high-quality thin films over two-dimensional (2D) as well as three-dimensional (3D) structures. Electrolyte membranes fabricated using ALD usually result in dense films with smoother surfaces free of pinholes.[7] Also, the relatively low deposition temperatures (typically <300°C) of ALD result in a microstructure with fine nanocrystalline grains (<10 nm) and hence a large grain-boundary density, which turns out to be beneficial for oxide-ion incorporation. The role of grain boundaries in oxygen exchange kinetics is discussed in the section on grain-boundary engineering.

Shim et al. demonstrated the fabrication of MEMS-based SOFCs using atomic layer deposited YSZ electrolyte for the first time.[6] They deposited YSZ by alternating ZrO$_2$ and Y$_2$O$_3$ cycles while controlling the doping ratio by varying the pulse ratio of the Zr- and Y-precursors (e.g., pulse ratio of ZrO$_2$:Y$_2$O$_3$ = 7:1 gives 8 mol% doped YSZ). Similarly, other researchers have also employed ALD to deposit YSZ electrolyte as thin as 50–80 nm.[4,8,11] Fan et al. demonstrated a MEMS-based bilayer electrolyte SOFC featuring a 70-nm-thick YSZ film with a 10-nm-thick YDC overlayer, all deposited by ALD.[37,38] They achieved a 14 mol% doping level for YDC using a 6:1 pulse ratio of CeO$_2$:Y$_2$O$_3$. Similarly, for the fabrication of proton-conducting oxides using ALD, Shim et al. successfully achieved the deposition of dense BZY thin films (~60 nm thick) by alternating pulses for BaO, ZrO$_2$, and Y$_2$O$_3$ precursors during ALD.[7,39] As ALD fabrication involves moderately low temperatures (usually <300°C) and pure metal-organic precursors of the metal cations, the resulting BZY films were dense and of high quality with no detectable impurities or secondary phases at grain boundaries. This is in contrast to the need for extremely high sintering temperatures typically exceeding 1400°C required to make dense BZY, which usually suffers from high grain-boundary resistance.[40]

These thin-film MEAs are intended for low-temperature studies, usually below 500°C, hence the choice of effective catalytic electrode materials, especially for ORR, is rather scarce. In this regard, Pt still reigns as the best catalytic electrode material for this temperature regime. Accordingly, porous Pt structures fabricated by thin-film deposition methods (e.g., sputtering, ALD) have been widely used (**Figure 2**).[3,41] Such porous Pt structures exhibit high catalytic activity as well as
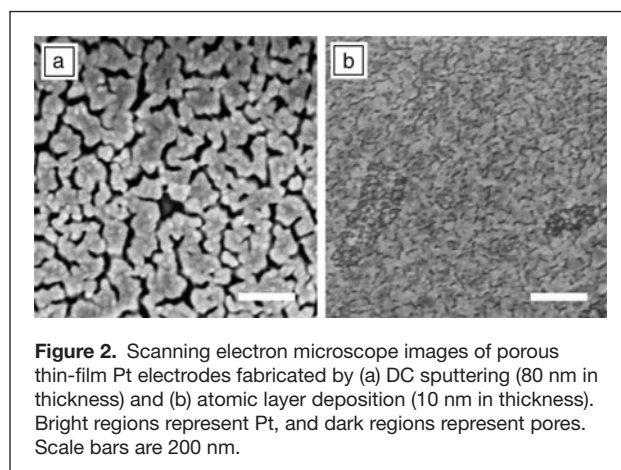

Figure 2. Scanning electron microscope images of porous thin-film Pt electrodes fabricated by (a) DC sputtering (80 nm in thickness) and (b) atomic layer deposition (10 nm in thickness). Bright regions represent Pt, and dark regions represent pores. Scale bars are 200 nm.

extremely low material loading (e.g., 0.02 mg cm^{-2}).[41] In addition, nanoscale pores ensure a high density of triple phase boundaries (i.e., the interface where electrode, electrolyte, and the gas phases meet), which play a crucial role in enabling high performance for MEMS-based SOFCs.

With nanoscale thin-film electrolytes, the contribution of the ohmic loss to the total cell losses becomes significantly smaller than that of the activation loss. For example, in MEMS-based SOFCs with ALD YSZ (50 nm) + PLD YDC (10 nm) bilayer electrolyte, the contribution of the ohmic loss to the total losses is <1% at OCV and <10% at a cell voltage of 0.5 V, respectively,[12] while the major portion of the remaining loss stems from the cathodic activation process for ORR. In this regard, understanding and engineering the cathode interface is extremely important to further enhance the performance of MEMS-based SOFCs, which can serve as an attractive testbed for exploring cathode interface engineering.

Grain-boundary engineering at the cathode interface
Role of surface grain boundaries
Nanoscale thin-film electrolytes employed in MEMS-based SOFCs usually have a large density of grain boundaries due to their fine-grain nature. It has been reported that grain boundaries at the cathode/electrolyte interface are of great importance in enhancing the oxygen reduction kinetics in SOFCs.[32,34,35,42] Oxide-ion incorporation is greatly facilitated by these surface grain boundaries. Thin-film electrolytes with high surface grain-boundary density consistently show higher exchange current density, j_0, than their single crystalline counterparts by several orders of magnitude due to the increase of j_0' in Equation 3 and, therefore, smaller activation loss as implied by Equation 2. This has been supported by experimental observations using secondary ion mass spectroscopy (SIMS) and electrochemical impedance spectroscopy (EIS).

Shim et al. used a NanoSIMS-50L instrument from Cameca, which performs SIMS with a lateral resolution of about 70 nm, to investigate the oxygen isotope exchange rate at surface grain boundaries of polycrystalline YSZ.[42] They annealed the polycrystalline YSZ in an $^{18}O_2$ environment so that the exchange reaction between ^{16}O inside YSZ and ^{18}O in the environment can take place. Surface mapping of ^{18}O and ^{16}O ions clearly indicates the preferential enrichment of ^{18}O along grain boundaries both under non-biased condition and cathodically biased conditions that imitate the cell voltage (**Figure 3**a and 3c). It is observed that the incorporation enhancement near the surface grain boundaries was not as prominent in the absence of an external bias as under cathodically biased conditions. This is because ORR tends to be driven more strongly by electrical potential, and therefore the oxide-ion incorporation rate is higher under electrical bias, accentuating the local differences in the oxide ion-incorporation rate. These results clearly demonstrate the active role of grain boundaries intersecting external surfaces of YSZ as preferential pathways for enhancing ORR.

Similarly, Kim et al. reported that oxygen exchange is enhanced along the grain boundaries at the surface of polycrystalline YDC.[35] This is depicted in Figure 3b and 3d, which shows NanoSIMS mapping of the ^{18}O versus ^{16}O concentrations on the surface of polycrystalline YDC. They confirmed that enhancement of oxygen exchange along surface grain boundaries is not a phenomenon unique to YSZ and doped ceria only, but is likely to be generalized to other fluorite structure oxides and possibly to perovskite oxides as well.[43,44]

Preferential exchange of oxygen at the surface grain boundaries causes the surface exchange coefficient or exchange current density at the nanocrystalline electrolyte surface to be significantly higher than that at the microcrystalline or single crystalline electrolyte surfaces. Huang et al. revealed that the surface exchange coefficient on an ALD-grown nanocrystalline
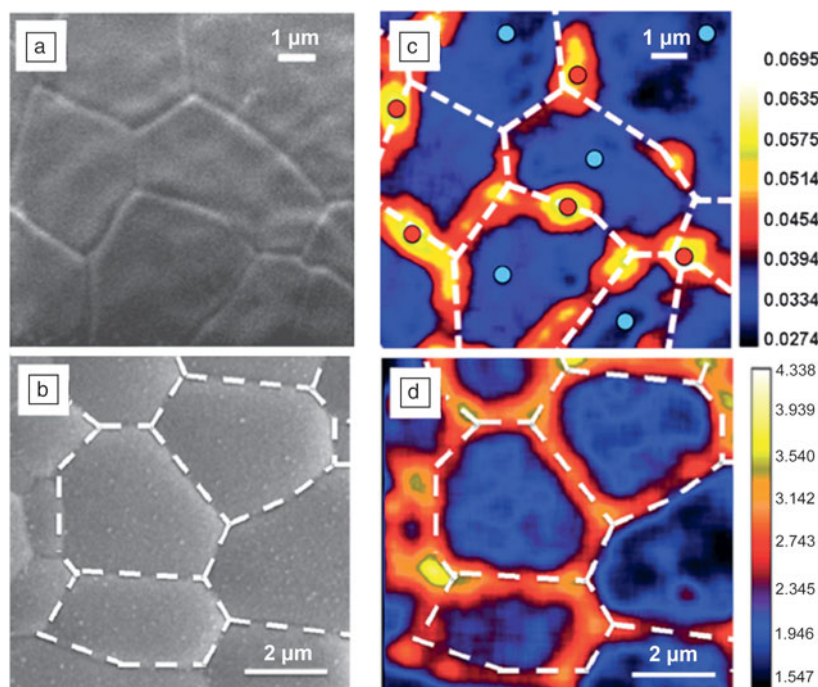

Figure 3. Scanning electron microscope image of (a) a polycrystalline yttria-stabilized zirconia (YSZ) surface and (b) a polycrystalline yttria-doped ceria (YDC) surface showing distinct grain boundaries. $^{18}O/^{16}O$ concentration obtained from secondary ion mass spectroscopy spatial scans of (c) the polycrystalline YSZ surface and (d) the polycrystalline YDC surface. Yellow and red indicate regions of a higher $^{18}O/^{16}O$ ratio that trace along the grain boundaries than the center-of-grains denoted by blue regions. Reprinted with permission from Reference 35, © 2011 Elsevier; and Reference 42, © 2012 Elsevier.

(grain size ~20 nm) YSZ surface is 2–3 times higher than that on a single crystalline YSZ(100) surface, using data extracted from the SIMS spectra.[43] Lee et al. compared the exchange current densities at the surfaces of nanocrystalline (grain size ~ hundreds of nanometers) and microcrystalline (grain size ~ a few micrometers) GDC films prepared by annealing at different temperatures (1100°C and 1400°C, respectively).[32] They found that the exchange current density at the nanocrystalline GDC surface is also 2–3 times higher than that at the microcrystalline GDC surface, which corresponds reasonably well to the result at the YSZ surface obtained by Huang. An and Kim also showed that the exchange current density at the nanocrystalline (grain size ~ tens of nanometers) YDC surface is several orders of magnitude higher than that at the microcrystalline YDC surface,[12] and the exchange current densities of nanocrystalline YDCs with slightly different grain sizes also differ from each other.[35] Interestingly, the exchange current density in YDC increases 2–3 times when the grain size is reduced from 52 ± 15 nm to 38 ± 2 nm.

The activation resistance, and the resulting activation loss, at the cathode interface is significantly reduced by an electrolyte surface featuring a high grain boundary density that facilitates a high surface exchange rate. Shim et al. systematically controlled the grain size of their as-deposited nanocrystalline YSZ thin films by thermal annealing.[42] EIS spectra revealed that the cathodic impedance decreases as the average grain size at the electrolyte surface increases. For example, the cathodic impedance at the surface of as-deposited PLD YSZ thin films (grain size ~50–60 nm) is approximately one order of magnitude smaller than that at the surface of annealed (at 1450°C) PLD YSZ thin films (grain size ~3–5 μm). Kim and Lee observed a similar trend for doped ceria.[32,34] For YDC, the cathodic impedance at the surface of as-deposited PLD YDC thin films (grain size ~40–70 nm) is 6–7 times smaller than that at the surface of annealed (at 1500°C) PLD YDC thin films (grain size ~5–7 μm). For GDC, the cathodic impedance at the surface of nanocrystalline sputtered GDC thin films (grain size ~ hundreds of nanometers) is ~2 times smaller than that at the surface of microcrystalline sputtered GDC thin films (grain size ~ a few micrometers).

Grain-boundary defect structure influences surface exchange

While it is clear that the cathodic activation loss decreases as the surface grain-boundary density increases, as discussed in the previous section, the activation energy for the cathode reaction kinetics does not change significantly with surface grain-boundary density. Indeed, the activation energies of cathodic kinetic processes at the YSZ surfaces of different size grains (50 nm to 5 μm) were reported to be similar to each other at 0.55 eV. Rather, the high concentration or segregation of the oxide-ion vacancies near the grain boundary seems to be responsible for the enhancement in oxide-ion incorporation.[42]

The segregation of oxide-ion vacancies near grain boundaries has been demonstrated at the atomic scale both in simulations and in experiments. Using hybrid Monte Carlo (MC)–molecular dynamics (MDs) simulations, Lee et al. showed that the oxide-ion vacancies segregate to the vicinity of grain-boundary cores ($\Sigma 5$ (310)/[001] symmetric tilt type), having a width of 1–2 nm in nanocrystalline YSZ and GDC.[45] Using Kelvin probe microscopy, Lee et al. experimentally confirmed that GDC surface grain boundaries are indeed charged positively by 100–150 mV with respect to the grain surface, providing indirect evidence for positively charged oxide-ion vacancies segregating preferentially to grain boundaries.[32] An et al. further investigated the oxide-ion vacancy segregation near the single $\Sigma 13$ (510)/[001] symmetric tilt grain boundary of bicrystal YSZ at atomic resolution using an aberration-corrected transmission electron microscope (**Figure 4**).[46,47] They quantified the occupancies of oxygen columns near the grain boundary using the negative spherical aberration (C_s) imaging technique, revealing that the oxygen columns at the grain-boundary core have a higher population of vacant sites than those away from the grain boundary, which has a core with a width of approximately 2 nm that corresponds well to the results from MC–MD simulations.

In parallel, Chao et al. demonstrated that a surface modification layer with a thickness of about 1 nm with enhanced oxide-ion vacancy concentration can improve the power density of a thin-film SOFC.[13,48] Chao et al. coated the cathode surface of the electrolyte with ALD YSZ of a higher doping level (14–19 mol%), beyond the optimal doping level for ionic conductivity (8 mol%). They observed a fivefold increase of the surface exchange coefficient, which corresponds well to the enhanced oxygen exchange on surfaces with high oxide-ion vacancy concentration.
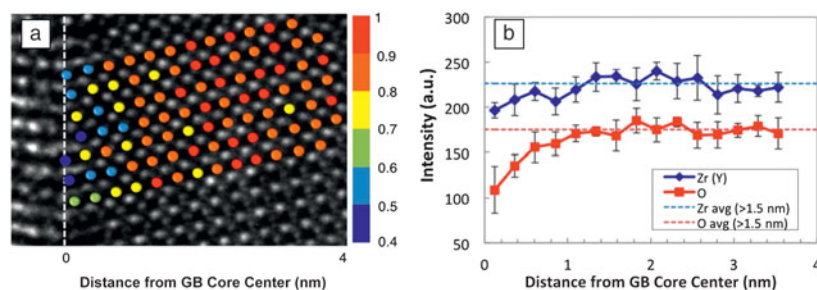

Figure 4. (a) Aberration-corrected transmission electron microscope image across a $\Sigma 13$ (510)/[001] symmetric tilt grain boundary (GB) (vertical dotted line) of a yttria-stabilized zirconia bicrystal at negative-C_s imaging conditions with oxygen columns in color code corresponding to their normalized image intensity (normalized by maximum oxygen column intensity). (b) Intensities of individual atomic columns corresponding to the occupancies of the columns. Reprinted with permission from Reference 46. © 2013 Nature Publishing Group.

Engineering of three-dimensional MEAs

Another way to improve cell performance is to spread the exchange current density, j_0, over a larger active cell area, thereby reducing the activation loss. Indeed, high surface area MEAs can be fabricated from 3D structured templates and thereby increase A/A' in Equation 3. Depending on the structure and dimensions of the underlying templates on which the MEA components are fabricated, area enhancement factors (i.e., A/A') ranging from 2 to 20 can be achieved.

Chao et al. first demonstrated a corrugated MEA architecture based on an ALD YSZ electrolyte (80 nm thick), which was deposited on a template fabricated by nanosphere lithography (NSL).[8] They used a wafer-scale self-assembly nanotexturing technique to pattern the silicon wafer, and the pattern was transferred to the MEA. They were able to form close-packed patterns without using conventional lithography techniques, and effectively enhanced the surface area by a factor of 1.6–2. Consequently, the exchange current density of the corrugated MEA showed approximately a twofold increase compared to that of the planar MEA. The enhancement in the exchange current density was in good agreement with the geometric enhancement of the active cell area. The activation loss therefore decreased by 30%, and the maximum power density increased from 0.56 W cm^{-2} (planar) to 0.82 W cm^{-2} (corrugated) at 450°C. An et al. reported that a similar approach can be applied to fabricate a MEA featuring a PLD YDC (10 nm) + ALD YSZ (50 nm) bilayer electrolyte (**Figure 5**a).[12] Compared to the planar YDC + YSZ bilayer MEA, they observed a 1.8-fold enhancement in the maximum power density that corresponds well to the area enhancement factor. Using this 3D MEA architecture, they were able to achieve 1.3 W cm^{-2} at 450°C, which represents the highest power density reported so far at this temperature.

Patterning methods using NSL were also employed to fabricate 3D MEAs featuring protonic conducting thin-film BZY electrolyte membranes deposited by PLD.[9] The BZY electrolyte membranes successfully covered the 3D structured template, and the resulting MEA showed ~1.5-fold increase in the maximum power density compared to its planar counterpart, demonstrating up to 186 mW cm^{-2} at 450°C using hydrogen as fuel.

Su et al. observed the behavior of a cup-shaped MEA with ALD YSZ electrolyte fabricated on a patterned silicon wafer using photolithography (Figure 5b).[4] This structure exhibited an array of cup-shaped trenches with a diameter of 15 μm and a depth of 10–40 μm, which resulted in an increase of electrochemically active sites per projected unit area by a factor of about 5. Even though the actual power density enhancement was only twofold compared to the planar one, possibly due to non-uniformity of the electrode layer deposited by sputtering and the imperfect removal of the underlying SiN layer, the activation loss was effectively reduced, resulting in a high maximum power density of 0.86 W cm^{-2} at 450°C.

Although far removed from conventional MEMS processing, aqueous electrodeposition and electro-dissolution methods can also be employed to fabricate 3D SOFC MEAs. For example, using these methods, Motoyama et al. demonstrated a nanotubular array of MEAs made of a one-end-closed hollow tube Ni/ALD YSZ/Pt (Figure 5c).[27] The dimensions of the tubular MEAs were ~5 μm in length and <500 nm in width (outside diameter) with a total MEA thickness of approximately 50 nm, which resulted in an area enhancement factor of about 20. Motoyama achieved a low OCV of 0.66 V with H_2 fuel and an extremely low maximum power density of 1.3 μW cm^{-2} at 550°C, possibly due to chemical shorting between the anode and cathode through hollow tubes. Nevertheless, such exceptionally high enhancement factors may represent a pathway toward achieving high power density in ultrathin SOFCs operating at intermediate to low temperatures.

Conclusions

MEMS and other microprocessing techniques are effective tools compatible with thin-film MEA fabrication methodologies that help expand SOFC architectures to beyond planar geometries and to low operating temperatures. More importantly, these thin-film MEAs serve as excellent platforms to investigate and elucidate electrode rate processes well separated from ohmic losses. Related examples were discussed to illustrate the impact of microstructure control at the nanoscale, particularly of grain size and surface grain-boundary density, where it was shown that increased grain-boundary density at the electrolyte/cathode interface improves the ORR kinetics at the cathode interface. Moreover, the 3D architecture of SOFC MEAs offers the capacity to significantly increase the active cell area, thereby resulting in improved cell performance. Long-term stability of these MEAs (e.g., due to degradation of electrodes[41,49]) is uncertain and yet to be verified. Materials properties as well as cell operating conditions will also impact MEA durability. Although the prospects of thin-film SOFCs for practical applications may be uncertain in spite of recent demonstrations of scaled-up MEAs,[5,19] they nevertheless serve as excellent testbeds for fuel cell research.
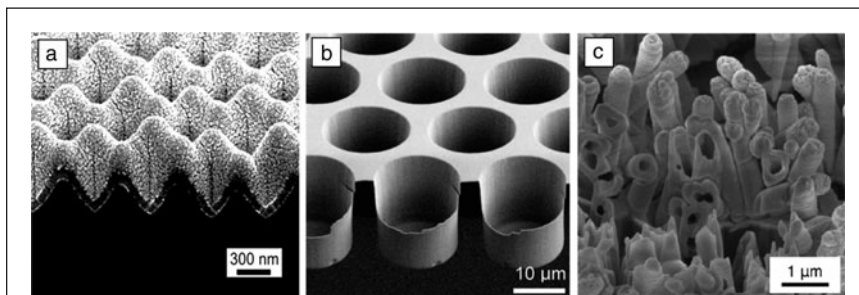

Figure 5. Images of three-dimensional micro-solid-oxide fuel cell architectures demonstrated with fully functional membrane electrode assemblies in (a) corrugated, (b) cup-shaped, and (c) nanotubular structures. Reprinted with permission from Reference 12, © 2013 American Chemical Society; Reference 4, © 2008 American Chemical Society; and Reference 27, © 2014 American Chemical Society.

References

1. R. O'Hayre, S.W. Cha, W. Colella, F.B. Prinz, *Fuel Cell Fundamentals* (2nd edition) (Wiley, NJ, 2009).
2. S.B. Adler, *Chem. Rev.* **104**, 4791 (2004).
3. H. Huang, M. Nakamura, P. Su, R. Fasching, Y. Saito, F.B. Prinz, *J. Electrochem. Soc.* **154**, B20 (2007).
4. P.-C. Su, C.-C. Chao, J.H. Shim, R. Fasching, F.B. Prinz, *Nano Lett.* **8**, 2289 (2008).
5. P.-C. Su, F.B. Prinz, *Electrochem. Commun.* **16**, 77 (2012).
6. J.H. Shim, C.-C. Chao, H. Huang, F.B. Prinz, *Chem. Mater.* **19**, 3850 (2007).
7. J.H. Shim, J.S. Park, J. An, T.M. Gür, S. Kang, F.B. Prinz, *Chem. Mater.* **21**, 3290 (2009).
8. C.-C. Chao, C.-M. Hsu, Y. Cui, F.B. Prinz, *ACS Nano* **5**, 5692 (2011).
9. Y.B. Kim, T.M. Gür, S. Kang, H.-J. Jung, R. Sinclair, F.B. Prinz, *Electrochem. Commun.* **13**, 403 (2011).
10. P.-C. Su, F.B. Prinz, *Microelectron. Eng.* **88**, 2405 (2011).
11. Z. Fan, J. An, A. Iaucu, F.B. Prinz, *J. Power Sources* **218**, 187 (2012).
12. J. An, Y.B. Kim, J. Park, T.M. Gür, F.B. Prinz, *Nano Lett.* **13**, 4551 (2013).
13. C.-C. Chao, J.S. Park, X. Tian, J.H. Shim, T.M. Gür, F.B. Prinz, *ACS Nano* **7**, 2186 (2013).
14. Y. Tang, K. Stanley, J. Wu, D. Ghosh, J. Zhang, *J. Micromech. Microeng.* **15**, S185 (2005).
15. A. Evans, A. Bieberle-Hütter, J.L.M. Rupp, L.J. Gauckler, *J. Power Sources* **194**, 119 (2009).
16. A.C. Johnson, B.-K. Lai, H. Xiong, S. Ramanathan, *J. Power Sources* **186**, 252 (2009).
17. Y. Takagi, B.-K. Lai, K. Kerman, S. Ramanathan, *Energy Environ. Sci.* **4**, 3473 (2011).
18. B.-K. Lai, K. Kerman, S. Ramanathan, *J. Power Sources* **196**, 6299 (2011).
19. M. Tsuchiya, B.-K. Lai, S. Ramanathan, *Nat. Nanotechnol.* **6**, 282 (2011).
20. J.H. Joo, G.M. Choi, *J. Power Sources* **182**, 589 (2008).
21. U.P. Muecke, D. Beckel, A. Bernard, A. Bieberle-Hutter, S. Graf, A. Infortuna, P. Müller, J.L.M. Rupp, J. Schneider, L.J. Gauckler, *Adv. Funct. Mater.* **18**, 1 (2008).
22. S. Kang, P. Heo, Y.H. Lee, J. Ha, I. Chang, S.W. Cha, *Electrochem. Commun.* **13**, 374 (2011).
23. Y.-I. Park, P.C. Su, S.W. Cha, Y. Saito, F.B. Prinz, *J. Electrochem. Soc.* **153**, A431 (2006).
24. C.-W. Kwon, J.-W. Son, J.-H. Lee, H.-M. Kim, H.-W. Lee, K.-B. Kim, *Adv. Funct. Mater.* **21**, 1154 (2011).
25. C.-W. Kwon, J.-I. Lee, K.-B. Kim, H.-W. Lee, J.-H. Lee, J.-W. Son, *J. Power Sources* **210**, 178 (2012).
26. S.B. Ha, P.-C. Su, S.W. Cha, *J. Mater. Chem. A* **1**, 9645 (2013).
27. M. Motoyama, C.-C. Chao, J. An, H.J. Jung, T.M. Gür, F.B. Prinz, *ACS Nano* **8**, 340 (2014).
28. K. Kerman, B.-K. Lai, S. Ramanathan, *Adv. Energy Mater.* **2**, 656 (2012).
29. D. Beckel, A. Bieberle-Hütter, A. Harvey, A. Infortuna, U.P. Muecke, M. Prestat, J.L.M. Rupp, L.J. Gauckler, *J. Power Sources* **172**, 325 (2007).
30. J.H. Shim, S. Kang, S.W. Cha, W. Lee, Y.B. Kim, J.S. Park, T.M. Gür, F.B. Prinz, C.-C. Chao, J. An, *J. Mater. Chem. A* **1**, 12695 (2013).
31. K. Kerman, S. Ramanathan, *J. Mater. Res.* **29**, 320 (2014).
32. W. Lee, H.J. Jung, M.H. Lee, Y.-B. Kim, J.S. Park, R. Sinclair, F.B. Prinz, *Adv. Funct. Mater.* **22**, 965 (2012).
33. Y.B. Kim, T.P. Holme, T.M. Gür, F.B. Prinz, *Adv. Funct. Mater.* **21**, 4684 (2011).
34. Y.B. Kim, J.H. Shim, T.M. Gür, F.B. Prinz, *J. Electrochem. Soc.* **158**, B1453 (2011).
35. Y.B. Kim, J.S. Park, T.M. Gür, F.B. Prinz, *J. Power Sources* **196**, 10550 (2011).
36. K. Bae, D.Y. Jang, H.J. Jung, J.W. Kim, J.-W. Son, J.H. Shim, *J. Power Sources* **248**, 1163 (2014).
37. Z. Fan, F.B. Prinz, *Nano Lett.* **11**, 2202 (2011).
38. Z. Fan, C.-C. Chao, F. Hossei-Babaei, F.B. Prinz, *J. Mater. Chem.* **21**, 10903 (2011).
39. J. An, Y.B. Kim, J.S. Park, J.H. Shim, T.M. Gür, F.B. Prinz, *J. Vac. Sci. Technol. A* **30**, 01A161 (2012).
40. P. Babilo, S.M. Haile, *J. Am. Ceram. Soc.* **88**, 2362 (2005).
41. J. An, Y.B. Kim, F.B. Prinz, *Phys. Chem. Chem. Phys.* **15**, 7520 (2013).
42. J.H. Shim, J.S. Park, T.P. Holme, K. Crabb, W. Lee, Y.B. Kim, X. Tian, T.M. Gür, F.B. Prinz, *Acta Mater.* **60**, 1 (2012).
43. T. Horita, K. Yamaji, N. Sakai, H. Yokokawa, T. Kawada, T. Kato, *Solid State Ionics* **127**, 55 (2000).
44. J. Fleig, *Annu. Rev. Mater. Res.* **33**, 361 (2003).
45. H.B. Lee, F.B. Prinz, W. Cai, *Acta Mater.* **61**, 3872 (2013).
46. J. An, J.S. Park, A.L. Koh, H.B. Lee, H.J. Jung, J. Schoonman, R. Sinclair, T.M. Gür, F.B. Prinz, *Sci. Rep.* **3**, 2680 (2013).
47. J. An, A.L. Koh, J.S. Park, R. Sinclair, T.M. Gür, F.B. Prinz, *J. Phys. Chem. Lett.* **4**, 1156 (2013).
48. C.-C. Chao, Y.B. Kim, F.B. Prinz, *Nano Lett.* **9**, 3626 (2009).
49. T. Ryll, H. Galinski, L. Schlagenhauf, P. Elser, J.L.M. Rupp, A. Bieberle-Hütter, L.J. Gauckler, *Adv. Funct. Mater.* **21**, 565 (2011).